JOTCS A
Journal of the Turkish Chemical Society
Section: A
Chemistry
TURKISH CHEMICAL SOCIETY

Electronic Diversity and Charge-Transport Properties of DPP Semiconductors: A Comparative DFT/TD-DFT Study

Pınar Seyitdanlıoğlu[1*], Hilal Kalkan[2]

[1]Hacettepe University, Faculty of Science, Department of Chemistry, Ankara, 06800, Türkiye.
[2]Gazi University, Rectorate, Ankara, 06500, Türkiye.

Abstract: Diketopyrrolopyrrole (DPP)-based semiconductors represent a versatile class of π-conjugated materials whose optoelectronic behavior can be effectively tuned through terminal-skeleton engineering. In this work, we present a comparative DFT/TD-DFT investigation of ten DPP derivatives in order to clarify how structural variation governs their electronic structure, optical response, excited-state character, and charge-transport tendencies. Benchmark calculations performed against the experimental frontier orbital energies of **C10** identified B3PW91/6-31+G(d,p) as the most suitable computational level for the studied series. The results show that most compounds retain largely planar backbones, whereas localized torsional variations act as important modulators of conjugation. The calculated HOMO and LUMO energies span from −4.99 to −5.64 eV and from −2.74 to −3.95 eV, respectively, revealing substantial electronic diversity across the molecular set. TD-DFT analysis indicates that **C8** is a promising candidate for near-infrared photodetection due to its narrow bandgap and pronounced charge-transfer character. Within the donor-relevant subset, **C9** emerges as the most balanced photovoltaic candidate, combining favorable donor-side energetic alignment with a strong optical response, whereas C10 exhibits a more pronounced electron-transport tendency due to its relatively low electron reorganization energy. By combining intrinsic CT/LE contributions with the Δr and Λ descriptors, the present study distinguishes formal donor–acceptor polarization from genuinely spatially separated charge-transfer excitation. Overall, this work provides a consistent structure–property framework for the evaluation and design of DPP-based organic semiconductors.

Keywords: Diketopyrrolopyrrole (DPP), DFT/TD-DFT, Electronic Diversity, Structure–Property Relationships, Charge Transport.

Submitted: March 28, 2026. **Accepted:** April 14, 2026.

Cite this: Seyitdanlıoğlu P, Kalkan H. Electronic Diversity and Charge-Transport Properties of DPP Semiconductors: A Comparative DFT/TD-DFT Study. JOTCSA. 2026, **1918166**, 1-16.

DOI: https://doi.org/10.18596/jotcsa.1918166

Izlik page: https://izlik.org/JA49GW63HY

***Corresponding author's E-mail:** pinarseyit@gmail.com

1. INTRODUCTION

The global commitment to achieving net-zero emissions has fundamentally shifted energy paradigms toward sustainable technologies, positioning organic electronics as a cornerstone of next-generation innovation (1). Within this framework, π-conjugated organic semiconductors have emerged as compelling alternatives to traditional silicon-based devices due to their mechanical flexibility, lightweight nature, and compatibility with cost-effective large-area fabrication (2,3). While significant breakthroughs in donor–acceptor (D-A) molecular design have pushed the performance of organic photovoltaics (OPVs), organic field-effect transistors (OFETs) (4) and photodetectors (5) to unprecedented levels, further advancement remains critically dependent on a fundamental understanding of how subtle structural modifications dictate energy-level alignment, optical absorption, and charge transport dynamics (6,7). The intricate interplay between molecular frontier orbitals and the resulting thin-film architecture governs the performance of these optoelectronic devices. Consequently, elucidating the structure-property relationships of versatile building blocks such as diketopyrrolopyrrole (DPP) is essential for tailoring materials for specific optoelectronic applications.

Among the diverse library of organic chromophores, diketopyrrolopyrrole (DPP) derivatives have emerged as exceptionally robust and versatile building blocks for high-performance optoelectronic applications (8,9). The core structure of DPP features a planar, highly conjugated π-system flanked by two carbonyl-

imide units, which confer strong electron-withdrawing character, high photochemical stability, and favorable π-π stacking interactions (10,11). This unique balance of electronic deficiency and structural rigidity allows the DPP scaffold to be strategically engineered for diverse optoelectronic roles; depending on peripheral functionalization and the nature of the conjugated spacers, these molecules can function effectively as either electron donors or non-fullerene acceptors (NFAs) (12,13). Furthermore, systematic modifications of π-bridges (e.g., thienyl, furanyl, or phenyl groups) and terminal end-groups enable precise fine-tuning of the absorption spectrum from the visible region to the near-infrared (NIR) edge, making these materials ideal candidates for tandem solar cells and indoor light-harvesting applications (14-16).

Despite the wealth of experimental data available in the literature, a direct and meaningful comparison between different DPP-based materials remains a significant challenge. These materials are often synthesized and reported under disparate device architectures, varying processing conditions, and different solvent environments, all of which can obscure their intrinsic electronic potential and hinder the development of a unified design logic for next-generation semiconductors. In this context, density functional theory (DFT) and its time-dependent extension (TD-DFT) provide a powerful and internally consistent framework for disentangling intrinsic electronic effects from external morphological and device-dependent variables (17-19). Within such a framework, frontier orbital energies and distributions, optical response, excited-state character, and intrinsic charge-transport tendencies can be evaluated on a common basis, enabling a more reliable comparison of structurally diverse DPP derivatives.

In this work, we present a systematic and comparative computational investigation of ten selected DPP derivatives (**C1**–**C10**) to evaluate their overall optoelectronic properties (10-29). Unlike previous studies that often report these molecules in isolation or at varying computational levels, our primary objective is to re-examine this diverse library within a consistent, synchronized theoretical framework. This approach allows for a direct, side-by-side comparison, bridging fragmented experimental observations with a unified structure-property perspective. We assess the electronic diversity of these compounds through their frontier orbital alignment, oscillator strengths, light-harvesting efficiencies (LHE), excited-state charge-transfer characteristics, and electron/hole reorganization energies. In particular, the nature of the low-lying excited states is examined using intrinsic charge-transfer/local-excitation (CT/LE) contributions, the Δr descriptor, and the λ-index, thereby distinguishing formal donor-acceptor polarization from genuinely spatially separated charge-transfer excitation. By benchmarking ten DPP derivatives under identical conditions, we clarify how terminal-skeleton engineering governs orbital alignment, optical absorption, excited-state behavior, and charge-transport tendency in DPP-based semiconductors. Ultimately, this study provides a consistent comparative framework for understanding how terminal-skeleton engineering governs the optoelectronic behavior of DPP-based semiconductors and for guiding the future design of application-specific materials.

2. COMPUTATIONAL METHODOLOGY

All quantum-chemical calculations were carried out using Gaussian 16 (30), while all molecular visualizations were prepared using GaussView 6 (31).

The electronic properties were evaluated from the optimized ground-state structures. HOMO and LUMO energies were obtained from the optimized geometries. The HOMO-LUMO gap was determined from the energy difference between the frontier orbitals. On this basis, the photovoltaic descriptors were estimated. The open-circuit voltage (V_{oc}) was calculated relative to PCBM as the reference acceptor using the commonly employed donor-acceptor energy-level expression (32):

$$V_{oc} = \left|E_{HOMO}^{donor}\right| - \left|E_{LUMO}^{acceptor}\right| - 0.3\,V \quad \text{(Eq. 1)}$$

where the empirical term of 0.30 eV accounts for interfacial energy losses. The normalized open-circuit voltage (nV_{oc}) and fill factor (FF) were then estimated from the calculated V_{oc} values using the following equations (33):

$$V_{oc} = \frac{qV_{oc}}{nk_BT}$$

$$\text{and } FF = \left[\frac{\frac{eV_{oc}}{k_BT} - \ln\left(\frac{eV_{oc}}{k_BT} + 0.72\right)}{\frac{eV_{oc}}{k_BT} + 1}\right] \quad \text{(Eq. 2)}$$

Since these photovoltaic descriptors were derived using PCBM as the reference acceptor, they were discussed primarily for compounds whose reported role and overall electronic behavior remained consistent with a donor-type photovoltaic framework.

The optical properties were investigated using TD-DFT calculations on the optimized ground-state geometries, with the conductor-like polarizable continuum model (CPCM) and dichloromethane as the solvent. The low-lying singlet excited states were used to obtain the excitation energies, oscillator strengths (f), and the corresponding maximum absorption wavelengths (λ_{max}). The light-harvesting efficiency (LHE) was estimated from the oscillator strength according to (34):

$$LHE = 1 - 10^{-f} \quad \text{(Eq. 3)}$$

Thus, the reported absorption-related properties were evaluated in an implicit dichloromethane environment to reflect the experimental optical conditions better.

The charge-transport tendency of the investigated compounds was further assessed through the calculation of electron and hole reorganization energies (λ_e and λ_h). These values were obtained from the total energies of the neutral, cationic, and

anionic species in both their optimized and nonequilibrium geometries using the standard expressions (35-37):

$$\lambda_e = \left(E_0^* - E_0\right) + \left(E_-^* - E_-\right)$$
$$\lambda_h = \left(E_0^* - E_0\right) + \left(E_+^* - E_+\right)$$

E_0 is the minimum energy of the neutral species at its own optimized geometry, while E_+ and E_- are the minimum energies of the cationic and anionic species, respectively, at their own optimized geometries. E_0^* denotes the single-point energy of the neutral species evaluated at the geometry of the cationic or anionic state, whereas E_+^* and E_-^* correspond to the single-point energies of the cationic and anionic species, respectively, calculated at the optimized neutral geometry. On this basis, the reorganization energies for electron and hole transfer were determined. To properly account for the need for diffuse functions in the charged species, the calculations were carried out using the unrestricted approach, and convergence as well as the verification of true minima were confirmed by frequency analyses.

To examine the nature of the excited states in greater detail, the Δr index, λ-index, and intrinsic charge-transfer/local-excitation (CT/LE) contributions were analyzed using Multiwfn (38). Because the intrinsic CT/LE percentages are sensitive to fragment definition, the final analysis was performed using chemically meaningful fragmentation schemes based on the major conjugated subunits and inter-ring junctions of each molecule rather than overly coarse partitioning. In the interpretation of excited-state character, the intrinsic CT contribution was therefore not considered alone, but was evaluated together with the Δr descriptor, which reflects the spatial separation between the hole and electron distributions, and the λ-index, which measures their degree of overlap. This combined approach made it possible to distinguish formal interfragment charge redistribution from genuinely spatially separated charge-transfer excitation.

Taken together, this computational protocol provided a unified framework for correlating molecular geometry, frontier orbital alignment, optical absorption, excited-state character, and intrinsic charge-transport behavior across the investigated DPP-based compounds.

3. RESULTS AND DISCUSSION

3.1. Benchmark Study for The Selection of The Computational Level

In order to determine the most appropriate theoretical level for the investigation of the target molecular series, a benchmark study was carried out by comparing the calculated frontier molecular orbital energies with the available experimental values for the reference compound **C10** (Table 1). Since the electronic structure of donor–acceptor systems is highly sensitive to the choice of exchange–correlation functional and basis set, the reliability of the computed HOMO and LUMO energies was first evaluated prior to the large-scale calculations. For this purpose, semi-empirical PM6 (39), range-separated hybrid ωB97XD/6-31G (40,41), conventional hybrid B3LYP with different basis sets (42), CAM-B3LYP/6-31G(d,p) (43,44), HSEH1PBE/6-31G(d,p) (45), PBEPBE/6-31G(d,p) (46,47), MPW1PW91/6-31G(d,p) (48), and B3PW91 (49) with several basis set combinations were tested. The experimental HOMO and LUMO energy levels of **C10** were reported as −5.20 and −3.40 eV, respectively, and these values were used as the main criteria for assessing the predictive performance of each computational approach.

The benchmark results clearly reveal that the tested methods exhibit markedly different performances in reproducing the experimental frontier orbital energies. The PM6 method significantly overestimated the stabilization of the HOMO level and strongly underestimated the LUMO energy, resulting in large deviations from experiment. Similarly, ωB97XD/6-31G produced a considerably deeper HOMO and a much less stabilized LUMO, indicating that this level is not suitable for the present system when accurate absolute orbital energies are targeted. The B3LYP family provided a more balanced description, yet the obtained HOMO and LUMO values still showed noticeable deviations from the experimental data. In contrast, CAM-B3LYP yielded an excessively low LUMO energy, which resulted in an unrealistic description of the frontier orbital distribution for the reference compound. HSEH1PBE and PBEPBE improved one orbital energy at the expense of the other, but neither method provided a sufficiently balanced agreement for both HOMO and LUMO levels simultaneously.

Among the methods examined, B3PW91-based calculations showed the most consistent agreement with experiment. In particular, the B3PW91/6-31+G(d,p) (49,50) level reproduced the experimental HOMO energy exactly (−5.20 eV, ΔHOMO = 0.00 eV) and provided a reasonably close LUMO value (−3.08 eV, ΔLUMO = 0.32 eV). Although B3PW91/6-311+G(d,p) also afforded comparable results, its improvement in LUMO deviation was only marginal, while the increased basis set size would lead to a higher computational cost for the full molecular set. A similar trend was also observed for B3PW91/6-311G(d,p) (49,51), which gave a very small HOMO deviation but did not outperform B3PW91/6-31+G(d,p) in a practically meaningful way. Therefore, the inclusion of diffuse functions in the 6-31+G(d,p) basis set appears to provide an appropriate balance between accuracy and efficiency for describing the frontier electronic structure of the studied molecules.

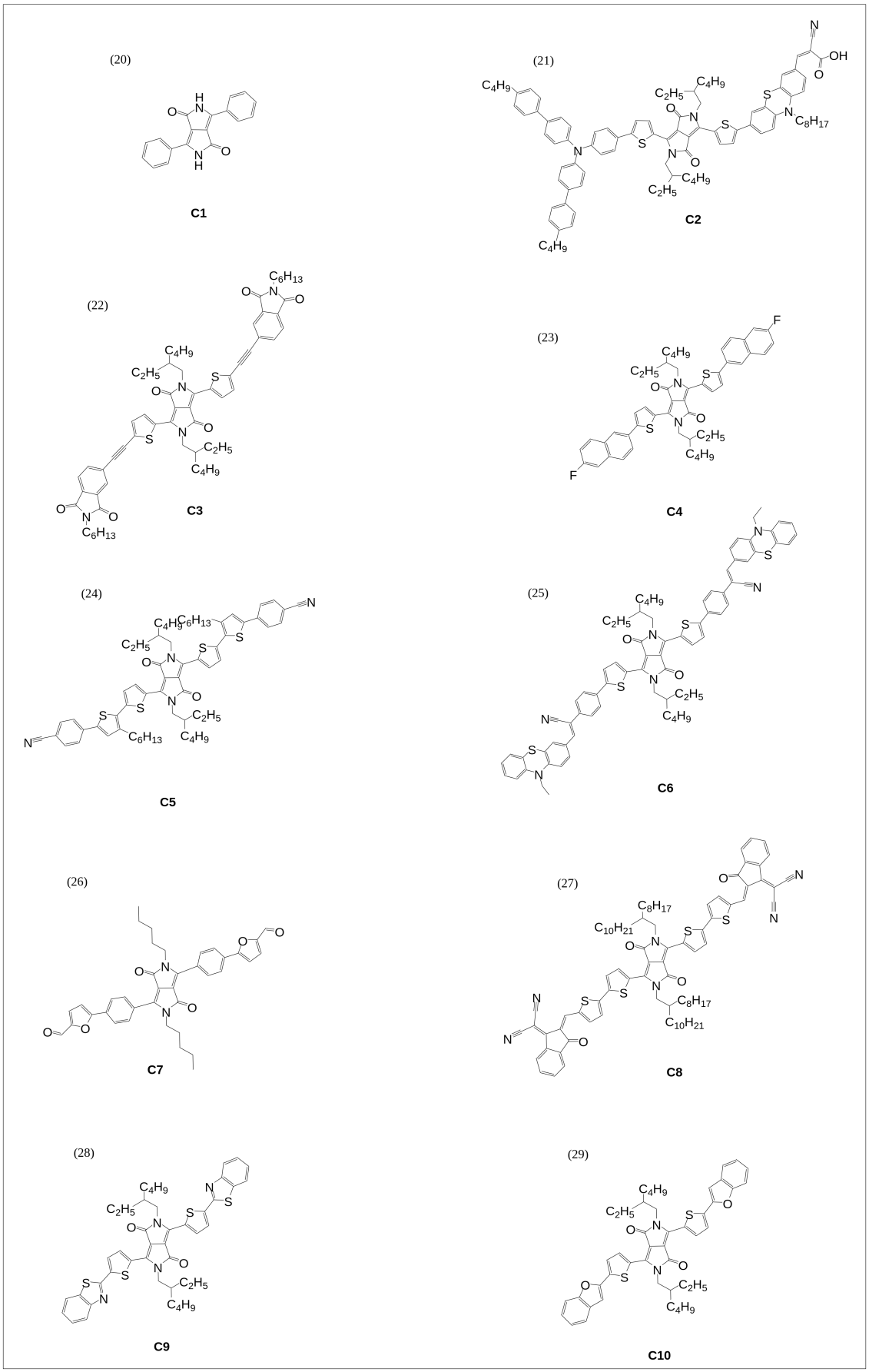

Figure 1: Selected DPP-based compounds (20-29).

On the basis of these findings, B3PW91/6-31+G(d,p) was selected as the optimum computational level for the subsequent geometry optimizations and electronic structure calculations of the entire molecular series. This choice is further justified by the need to use a single, internally consistent theoretical framework for all derivatives to ensure meaningful comparisons of substituent effects,

orbital energy shifts, and structure–property relationships across the dataset. Overall, the benchmark analysis demonstrates that B3PW91/6-31+G(d,p) offers the most reliable compromise between computational cost and agreement with experiment, making it a suitable level of theory for the systematic evaluation of the designed donor–acceptor compounds.

Table 1: Benchmark study for **C10** molecule (all energies in eV).

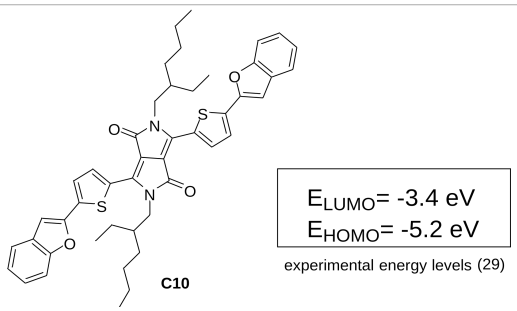

Functional	Basis Set	HOMO	LUMO	ΔHOMO	ΔLUMO
Semi-empirical	PM6	-9.50	-1.82	-4.30	1.58
WB97XD	6-31G	-6.92	-1.36	-1.72	2.04
B3LYP	6-31G	-5.01	-2.97	0.19	0.43
B3LYP	6-31G(d)	-4.87	-2.77	0.33	0.63
B3LYP	6-31G(d,p)	-4.88	-2.78	0.32	0.62
CAM-B3LYP	6-31G(d,p)	-6.11	-2.39	-0.91	1.01
B3PW91	6-31G(d,p)	-4.99	-2.88	0.21	0.52
HSEH1PBE	6-31G(d,p)	-4.74	-3.05	0.46	0.35
PBEPBE	6-31G(d,p)	-4.32	-3.23	0.88	0.17
MPW1PW91	6-31G(d,p)	-5.12	-2.74	0.08	0.66
B3PW91	6-311G(d,p)	-5.18	-3.04	0.02	0.36
B3PW91	6-31+G(d,p)	-5.20	-3.08	0.00	0.32
B3PW91	6-311+G(d,p)	-5.23	-3.10	-0.03	0.30

3.2. Molecular Geometry

Before discussing the optimized geometries of the full molecular set, the preferred orientation of the thiophene rings relative to the DPP core was examined using the model **Ty–DPP–Ty** system. A relaxed potential energy scan followed by PM6 semi-empirical scan analysis showed that the conformation in which both thiophene rings adopt the same orientation relative to the DPP carbonyl groups is energetically more favorable (Supplementary information Figure S1). This preference can be attributed to a more favorable interaction between the carbonyl oxygen atoms and the β-hydrogen atoms of the thiophene rings, whereas the alternative orientation involves less favorable repulsive interactions. This tendency was also reflected in the optimized geometries of the investigated molecules, where the DPP and adjacent thiophene units generally adopted similar relative orientations. All compounds were optimized at the B3PW91/6-31+G(d,p) level of theory. Atom numbering schemes and bond lengths and dihedral angles for optimized structures are given in Supplementary information Table S1-Table S10. Optimized structures of **C1**, **C7**, **C8**, and C9 are shown in Figure 2, and all optimized structures are shown in Figure S2.

The optimized structure of **C1** displays an almost symmetric geometry around the DPP core. The bond lengths within the terminal phenyl rings fall in the expected aromatic range, while the C5–C6 and C7–C8 bonds (1.38 and 1.38 Å, respectively) are shorter than the central C6–C7 bond (1.43 Å), indicating the bond-length alternation characteristic of the conjugated DPP framework. In addition, the C4–C5 and C8–C9 bonds are both 1.46 Å, consistent with single-bond character at the phenyl–DPP junctions. The dihedral angles φ_1 and φ_2 were calculated to be 29.62° and 30.00°, respectively, indicating that both phenyl rings are similarly twisted relative to the DPP core. This moderate torsion suggests partial preservation of conjugation despite the non-planar arrangement.

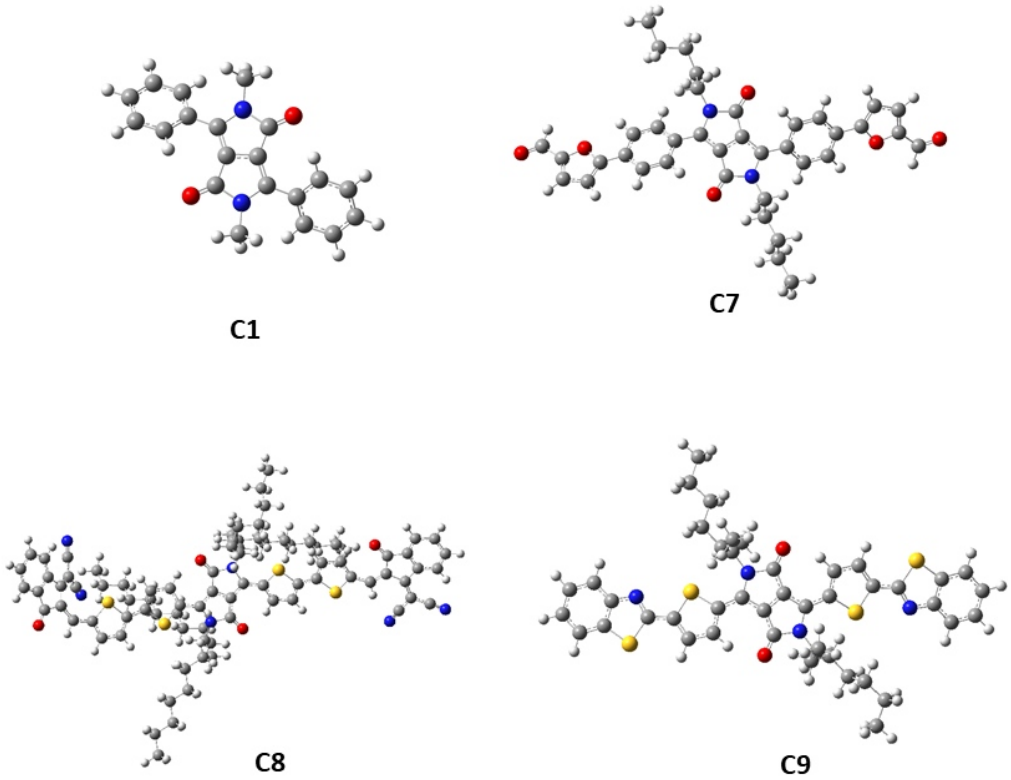

Figure 2: Optimized structures of **C1**, **C7**, **C8** and **C9** molecules at B3PW91/6-31+G(d,p) theory level.

The optimized structure of **C2** shows a non-uniform torsional profile along the conjugated backbone. The terminal diarylamine side is noticeably twisted, with dihedral angles of −38.80° for φ_1 and −43.84° for φ_2, indicating limited coplanarity in this part of the molecule. By contrast, the thiophene units adjacent to the DPP core are almost planar, as reflected by the small φ_4 and φ_5 values of 5.93° and 5.51°, respectively, which favors conjugation through the central segment. The torsion angle decreases to −21.28° at φ_3 and remains moderate on the acceptor side with φ_6 = 24.54°, showing that the deviation from planarity is mainly localized at the peripheral aryl junctions rather than at the DPP-centered core. This is also consistent with the bond-length pattern, where the inter-ring C–C bonds such as C12–C13 (1.46 Å), C16–C17 (1.44 Å), C20–C21 (1.44 Å), and C24–C25 (1.46 Å) retain partial single-bond character, while the shorter bonds within the heteroaromatic fragments support the presence of effective π-delocalization along the central backbone.

The optimized structure of **C3** retains a largely planar geometry around the central DPP-based conjugated segment. The dihedral angle φ_1 (C11–C12–C13–C14) is only −2.58°, indicating an almost coplanar arrangement at one side of the DPP–thiophene junction, while φ_2 (C15–C16–C17–C18) is slightly larger at 16.80°, pointing to a minor twist on the opposite side. Overall, these values suggest that the backbone remains sufficiently planar for effective π-conjugation. The bond-length pattern also supports this interpretation: the short distances of 1.22 Å are characteristic of the acetylenic linkers, whereas the longer bonds around 1.49 Å correspond to the inter-ring single-bond connections. Together, these results show that **C3** adopts an extended, nearly planar π-conjugated framework, with only limited torsional distortion along the backbone.

The optimized structure of **C4** shows a partially planar backbone with torsional distortion mainly arising at the outer aryl–thiophene junctions. The DPP-centered segment remains relatively planar, as indicated by the small dihedral angles φ_2 (−3.66°) and φ_3 (17.35°), whereas the terminal fragments are more twisted, with φ_1 and φ_4 calculated as 26.31° and −26.70°, respectively. This suggests that conjugation is better preserved around the central core than at the peripheral regions. The bond-length pattern is consistent with this picture, with longer inter-ring bonds such as C5–C6 (1.46 Å) and C17–C18 (1.46 Å) reflecting single-bond character, while the shorter bonds within the thiophene-containing segments support continued π-delocalization along the backbone.

The optimized structure of **C5** exhibits an overall extended and nearly planar conjugated backbone. Although the terminal dihedral angles φ_1, φ_2, φ_5, and φ_6 are given as −157.49°, −164.83°, 158.67°, and −155.88°, these values correspond to an almost anti-coplanar arrangement rather than severe twisting. The central part of the molecule is even closer to planarity, with φ_3 and φ_4 of 17.33° and 17.71°, indicating only a slight deviation from coplanarity around the DPP-centered segment. The bond-length distribution supports this geometry: the terminal C≡N bonds (N1–C2 and C31–N32) are both 1.16 Å, consistent with nitrile groups, while the inter-ring bonds such as C6–C7 (1.46 Å), C10–C11 (1.44 Å), C14–C15 (1.44 Å), C18–C19 (1.44 Å), C22–C23 (1.44 Å), and C26–C27 (1.46 Å) retain predominant single-bond character. Overall, **C5** adopts a largely coplanar and well-extended geometry, which should favor

efficient π-electron delocalization along the molecular backbone.

The optimized structure of **C6** shows a largely planar DPP-centered backbone with only moderate twisting at the outer junctions. The dihedral angles φ_2 and φ_3 are 8.00° and 6.87°, indicating that the conjugated segment directly connected to the DPP core remains nearly coplanar, whereas φ_1 and φ_4 increase to 23.14° and −22.45° toward the terminal units. This suggests that the main deviation from planarity is confined to the peripheral fragments, while conjugation is largely maintained across the central part of the molecule. The bond-length distribution is in line with this picture, with longer inter-ring bonds such as C14–C15 (1.46 Å), C18–C19 (1.44 Å), C22–C23 (1.44 Å), and C26–C27 (1.46 Å) indicating predominant single-bond character at the linking positions, while the shorter bonds within the aromatic and thiophene units support effective π-delocalization along the backbone.

The optimized structure of **C7** adopts an almost anti-coplanar arrangement along most of the conjugated backbone. The terminal dihedral angles φ_1 and φ_4 are 179.36° and 178.91°, respectively, showing that the outer fragments are essentially coplanar with the adjacent rings. By contrast, φ_2 and φ_3 are −149.02° and −149.25°, indicating a moderate deviation from coplanarity at the DPP–aryl junctions. Thus, the main torsional distortion is localized around the central part of the molecule, while the terminal segments remain well aligned. The bond-length pattern is consistent with this geometry: the O1–C2 and C23–O24 distances of 1.22 and 1.22 Å confirm the presence of carbonyl groups, whereas the longer inter-ring bonds such as C2–C3 (1.45 Å), C6–C7 (1.45 Å), C10–C11 (1.46 Å), C14–C15 (1.46 Å), C18–C19 (1.45 Å), and C22–C23 (1.45 Å) reflect predominant single-bond character at the linking positions. Overall, **C7** preserves a largely extended conjugated framework despite moderate twisting near the central DPP core.

The optimized structure of **C8** shows a largely extended backbone with only limited torsional distortion around the DPP-centered conjugated path. The dihedral angles φ_2 and φ_3 are 13.30° and 13.10°, indicating that the segments directly attached to the DPP core remain close to coplanarity, while φ_1 and φ_4, with values of 170.32° and 179.29°, correspond to an almost anti-periplanar arrangement at the outer thiophene-linked fragments. This overall geometry suggests that π-conjugation is largely preserved throughout the molecular framework. The bond lengths also support this picture: the inter-ring bonds C10–C11, C14–C15, C18–C19, and C22–C23 are in the approximately 1.44 Å range, consistent with partial single-bond character at the linking positions, whereas the short C≡N distances of both 1.16 Å clearly confirm the presence of the terminal cyano groups. Overall, **C8** adopts a well-extended and nearly planar conformation that should be favorable for efficient electronic communication along the backbone.

The optimized structure of **C9** exhibits a highly ordered and nearly planar conjugated framework. The dihedral angles φ_2 and φ_3 are only 7.69° and 8.60°, showing that the segments directly connected to the DPP core remain almost coplanar, while φ_1 and φ_4 are 179.78° and 179.52°, respectively, corresponding to an essentially anti-periplanar arrangement at the terminal heteroaromatic units. This geometry indicates that the overall backbone is well aligned for effective π-conjugation. The bond-length pattern is also consistent with this structural feature: the inter-ring bonds C5–C6, C9–C10, C13–C14, and C17–C18 fall in the expected range for predominantly single-bond linkages within an extended conjugated system, whereas the shorter C4–C5 and C18–C19 distances (1.30 Å) point to enhanced double-bond character in the terminal heteroaromatic fragments. Overall, **C9** adopts a rigid, highly planar geometry that should facilitate efficient intramolecular charge delocalization.

The optimized structure of **C10** exhibits a largely planar and well-extended conjugated backbone. The outer fragments are essentially anti-coplanar, with φ_1 and φ_4 calculated as 179.80° and 179.86°, respectively, while the dihedral angles near the DPP core remain relatively small (φ_2 = −15.65° and φ_3 = −17.00°), indicating only a slight torsional distortion in the central part of the molecule. This geometry suggests that planarity is largely maintained throughout the backbone, which is favorable for π-conjugation. The bond-length distribution supports this interpretation, with inter-ring bonds such as C5–C6 (1.44 Å), C9–C10 (1.44 Å), C13–C14 (1.44 Å), and C17–C18 (1.44 Å) showing partial single-bond character, while the shorter C4–C5 and C18–C19 bonds (1.37 Å) indicate increased double-bond contribution within the terminal heteroaromatic units. Overall, **C10** adopts a rigid and nearly planar geometry that should facilitate effective intramolecular electronic delocalization.

3.3. Frontier Molecular Orbital Analysis

The frontier molecular orbital distributions of **C1–C10** indicate that the electronic structure is highly sensitive to the nature of the terminal fragments and the overall conjugated architecture (Supplementary information Table S11). In most cases, the HOMO is mainly distributed over the electron-rich aryl/thiophene segments together with the DPP-centered conjugated path, whereas the LUMO extends more strongly toward the electron-deficient part of the molecule. This general pattern is consistent with the donor-acceptor character of the selected DPP-based structures.

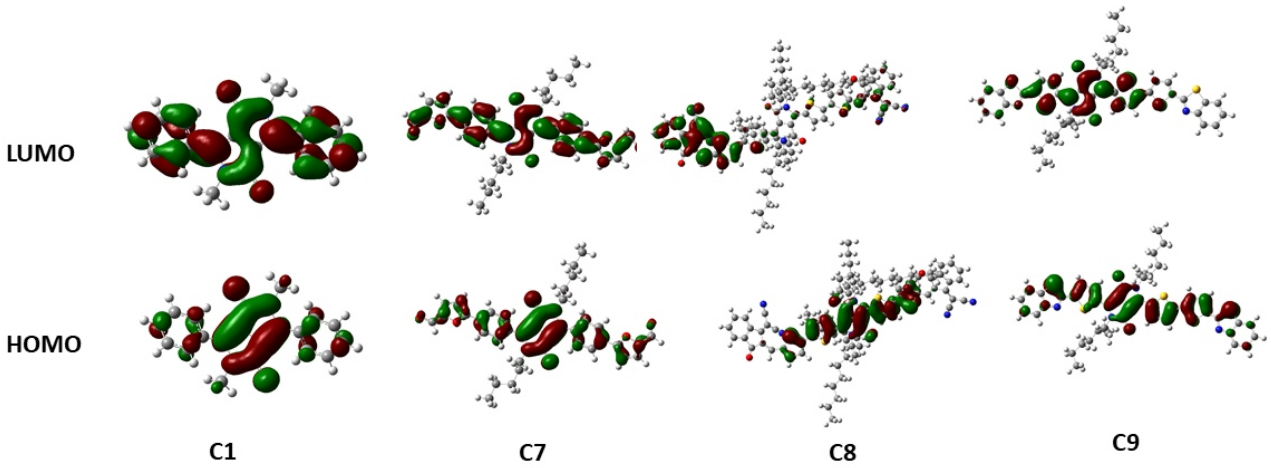

Figure 3: Calculated HOMO and LUMO contour diagrams of **C1**, **C7**, **C8** and **C9** at B3PW91/6-31+G(d,p) theory level.

Figure 3 presents calculated HOMO and LUMO contour diagrams of **C1**, **C7**, **C8** and **C9** at B3PW91/6-31+G(d,p) theory level. For **C1**, both the HOMO and LUMO remain largely concentrated on the DPP-centered core, while the terminal phenyl rings contribute only weakly, indicating relatively limited end-group conjugation. In **C2**, the orbital distribution becomes more asymmetric, with the HOMO more localized over the donor-rich side and the LUMO extending more effectively over the DPP-containing backbone and the opposite segment, suggesting a noticeable intramolecular redistribution of electron density upon excitation. A more balanced delocalization is observed for **C3** and **C4**, where both frontier orbitals are distributed across the central conjugated scaffold, indicating efficient electronic communication along the backbone.

The influence of stronger terminal electron-withdrawing groups becomes more evident in **C5, C8,** and **C10**. In these compounds, the LUMO shows a more pronounced contribution from the terminal acceptor fragments than the HOMO, indicating stronger acceptor-side participation in the low-lying virtual orbitals. This tendency is especially clear in **C8**, which exhibits the strongest terminal contribution to the LUMO and the most pronounced acceptor-side stabilization in the series. In **C6, C7,** and C**9**, the HOMO and LUMO remain comparatively well delocalized, although the LUMO still shows somewhat greater extension over the more electron-deficient segments. Overall, the orbital maps show that strengthening the terminal acceptor units promotes greater LUMO localization and enhances the spatial distinction between occupied and unoccupied frontier orbitals.

The calculated frontier orbital energies show that the selected DPP-based compounds span a fairly broad electronic range, with HOMO levels between −4.99 and −5.64 eV and LUMO levels between −2.74 and −3.95 eV (Table 2). Overall, the calculated data show reasonable consistency with the experimental values (Supplementary information Table S12). While some molecules show deviations approaching 0.5 eV, most compounds follow the same trend and remain within an acceptable agreement range. Considering that the calculated HOMO-LUMO gaps and experimentally derived optical gaps are not strictly equivalent quantities, the observed level of agreement supports the suitability of the B3PW91/6-31+G(d,p) methodology for comparative evaluation of this molecular set. As expected, both the nature of the terminal substituents and the extent of conjugative communication along the backbone play a decisive role in shaping the final energy-level alignment. In general, deeper HOMO levels are associated with improved oxidative stability and, in a donor-based device, potentially higher open-circuit voltages. In contrast, stronger LUMO stabilization leads to narrower band gaps and more red-shifted absorption (Supplementary information Figure S3).

Table 2: Calculated electronic and optical parameters of all molecules at B3PW91/6-31+G(d,p) theory level.

	HOMO(eV)	LUMO(eV)	$\Delta E_{H\text{-}L}$	f	λ_{max}	LHE
C1	-5.49	-2.74	2.75	0.50	486.67	0.68
C2	-4.99	-2.94	2.05	1.90	695.32	0.99
C3	-5.49	-3.49	2.00	1.95	692.33	0.99
C4	-5.20	-2.99	2.21	1.49	622.89	0.97
C5	-5.27	-3.21	2.06	1.78	653.76	0.98
C6	-5.08	-3.00	2.08	2.42	688.66	1.00
C7	-5.64	-3.24	2.40	1.20	577.78	0.94
C8	-5.59	-3.95	1.64	2.15	895.39	0.99
C9	-5.26	-3.25	2.01	1.58	663.93	0.97
C10	-5.17	-3.06	2.11	1.66	657.09	0.98

At one end of the series, **C1** exhibits the widest HOMO-LUMO gap (2.75 eV), arising from a relatively deep HOMO (−5.49 eV) combined with a weakly stabilized LUMO (−2.74 eV). This behavior is fully consistent with its more localized frontier orbital distribution, limited end-group participation, and overall weak donor-acceptor polarization. At the opposite extreme, **C8** displays the lowest LUMO level (−3.95 eV) and the smallest band gap (1.64 eV), clearly indicating the strongest acceptor-side stabilization in the present set. This result is also in line with its pronounced charge-transfer character and strongly red-shifted absorption. Compounds **C3**, **C5**, **C6**, **C9**, and **C10** occupy an intermediate energy window, with band gaps close to 2.00–2.11 eV, whereas C7 remains somewhat wider at 2.40 eV despite having the deepest HOMO of the whole set (−5.64 eV), because its LUMO is only moderately stabilized (−3.24 eV).

When the compounds are considered in terms of their broader electronic behavior, a single donor-acceptor classification is clearly inadequate for the entire series. **C1** is best regarded as a relatively localized, wide-gap member with weak donor-acceptor polarization. **C2** and **C7** occupy a more intermediate position, showing neither a clearly donor-like nor a strongly acceptor-dominated profile. By contrast, **C3**, **C5**, and especially **C8** are better described as acceptor-biased structures because of their stronger LUMO stabilization, narrower gaps, and more pronounced low-energy electronic response. In particular, **C3** combines a deep HOMO (−5.49 eV) with a markedly stabilized LUMO (−3.49 eV), while **C5** retains a somewhat less extreme but still clearly acceptor-favored balance (LUMO is −3.21 eV, $E_{H\text{-}L}$ is 2.06 eV). On the donor side, **C6**, **C9**, and **C10** remain the most relevant compounds for photovoltaic evaluation in a fullerene-referenced framework. Their HOMO levels (−5.08, −5.26, and −5.17 eV, respectively) are sufficiently deep to support reasonable voltage output, while their LUMO levels remain compatible with gaps near 2.0 eV. Among them, **C9** appears especially well balanced, combining a HOMO of −5.26 eV with a LUMO of −3.25 eV, whereas **C6** has the shallowest HOMO in this donor-oriented subset and therefore a less favorable voltage profile despite its strong optical response.

The frontier-orbital results indicate that the series does not follow a single electronic pattern. Some compounds remain relatively localized and wide-gap in character, whereas others achieve substantial LUMO stabilization, narrower gaps, and stronger donor-acceptor polarization. This diversity is important because it explains why the selected structures cannot all be discussed within exactly the same photovoltaic context, even though they belong to the broader DPP family.

The optical response follows a similarly differentiated pattern. Within the donor-relevant subset, **C6**, **C9**, and **C10** absorb at 688.66, 663.93, and 657.09 nm, respectively, showing that all three already extend well into the low-energy visible region. They do not, however, perform equally in terms of transition intensity. **C6** is particularly notable, exhibiting the highest oscillator strength of the entire series (f is 2.42) and, accordingly, the highest light-harvesting efficiency (LHE is 0.9962). This suggests that, although its frontier-level alignment is less favorable than that of **C9**, its light-harvesting ability is exceptionally strong. **C9** and **C10** also retain high optical efficiencies, with f values of 1.58 and 1.66 and LHE values of 0.97 and 0.98, respectively, indicating that they combine good transition probability with more balanced donor-side energetics.

A different optical profile is observed for the more acceptor-biased compounds. **C8** stands out most clearly, with a calculated λ_{max} of 895.39 nm, reflecting the strongest bathochromic shift in the whole set. Its very high oscillator strength (2.15) and LHE (0.99) further confirm that it is not only the most red-shifted absorber but also one of the most optically efficient compounds in the series. **C3** shows a similarly favorable low-energy response, with λ_{max} is 692.33 nm, f is 1.95, and LHE is 0.99, while **C5** also maintains a strong optical profile (653.76 nm, f is 1.78, LHE is 0.98). These acceptor-biased members are distinguished not only by stronger LUMO stabilization but also by a more favorable absorption profile in the low-energy region.

These optical trends are consistent with the frontier-orbital picture. The localized, wide-gap character of C1 leads to the shortest wavelength and weakest transition in the series; the intermediate compounds remain electronically mixed; the donor-relevant members preserve a balanced combination of HOMO depth and optical intensity; and the acceptor-biased structures—most notably **C8**—benefit from both stronger LUMO stabilization and markedly enhanced long-wavelength absorption.

Among the more acceptor-biased compounds, **C8** stands out most clearly. Its calculated λ_{max} reaches 895.39 nm, far beyond that of the rest of the series, and this behavior is fully consistent with its strongly stabilized LUMO level and very small energy gap. At the same time, it retains a very high oscillator strength (f is 2.15) and LHE (0.99), making it the most efficient absorber in terms of spectral coverage. Compound **C3** also shows a highly favorable optical profile, with a band gap of 2.00 eV, λ_{max}=692.33 nm, f is 1.9496, and LHE is 0.9888, whereas **C5** combines a somewhat less pronounced LUMO stabilization with still strong optical characteristics (λ_{max}=653.76 nm, f is 1.78, LHE is 0.98). Taken together, these results indicate that the acceptor-biased members of the series are not only more electronically polarized but also better positioned for low-energy absorption.

These trends are fully consistent with the excited-state descriptors discussed above. The more acceptor-biased compounds are characterized not only by lower LUMO energies, but also by stronger charge-transfer contributions and, in the case of **C8**, a much clearer spatial separation between the hole and electron distributions. By contrast, the donor-relevant compounds retain a more balanced combination of HOMO depth, optical response, and energetic alignment. The frontier-orbital and excited-state analyses therefore lead to the same conclusion: the present series contains electronically distinct subsets that should not be interpreted within a single, uniform donor-acceptor framework.

Since V_{oc}, normalized V_{oc}, FF, and especially ΔLUMO were estimated using PCBM as the reference

acceptor, these descriptors are most meaningfully discussed only for compounds whose reported role and overall electronic behavior remain consistent with a donor-type photovoltaic picture. In the present set, this condition is best satisfied by **C6, C9,** and **C10**. For the remaining compounds, particularly those showing stronger acceptor-biased character, the PCBM-referenced values may still be listed for completeness, but they should not be overinterpreted as definitive donor-performance indicators.

Among these donor-like compounds, **C9** shows the most balanced photovoltaic profile. C9 combines a V_{oc} of 0.658 V, a normalized V_{oc} of 25.41, an FF of 0.839, and the lowest ΔLUMO value among the three compounds (1.052). This combination suggests that **C9** offers the most favorable compromise between HOMO stabilization and donor-acceptor energetic alignment relative to PCBM. Its reasonably deep HOMO, together with a more moderate acceptor-side offset, makes it the most convincing donor candidate within this group.

C10 follows with a V_{oc} of 0.570 V, a normalized V_{oc} of 21.99, an FF of 0.821, and a ΔLUMO value of 1.238. Although its excited-state analysis indicates a more pronounced charge-transfer contribution than that of **C9**, its donor-side photovoltaic descriptors remain acceptable. **C10**, therefore, appears as a plausible donor-like candidate, albeit less balanced than **C9**.

A different situation is observed for **C6**. Despite its excellent optical response, it gives the lowest V_{oc} among the donor-like compounds (0.480 V), together with the highest ΔLUMO (1.295) and the lowest normalized V_{oc} (18.53). Its FF remains acceptable (0.797), but overall, its energetic alignment is less favorable than those of **C9** and **C10**. This indicates that **C6** is more notable for its very strong absorption and high light-harvesting efficiency than for its voltage-related photovoltaic descriptors.

Within the fullerene-referenced framework, the donor-like compounds show different levels of performance. **C9** emerges as the most balanced donor candidate, combining the most favorable donor-side energetic alignment with a consistently strong optical response. **C10** remains a viable donor-like system with reasonable overall photovoltaic behavior, whereas **C6** is better regarded as an optically excellent but energetically less favorable donor candidate. This distinction is important, as it shows that strong absorption alone is not sufficient to guarantee the most advantageous donor-side photovoltaic profile.

3.4. Excited-State Charge-Transfer Characteristics

To gain deeper insight into the nature of the low-lying excited states, the Δr index, λ-index, and intrinsic CT/LE percentages were evaluated collectively (Table 3). In addition, Transition Density Matrix (TDM) maps and Hirshfeld-partitioned hole-electron distributions were generated for the primary transitions (Figure 4 and Supplementary information Figure S4). These maps provide a spatial representation of the interaction between the ground and excited states, effectively distinguishing between localized excitations (LE) and intramolecular charge transfer (ICT) processes.

As illustrated in the TDM maps (Figure 4, top row), the electronic transition coherence varies significantly across the series. For **C1** and **C7**, the density is primarily concentrated along the diagonal, indicating a dominant LE character where the electron and hole remain spatially proximal. In contrast, **C8** displays significant off-diagonal contributions, complemented by a distinct spatial separation in the hole-electron isosurface plots (Figure 4, bottom row). In these visualizations, the blue regions (hole) and green regions (electron) exhibit a marked shift toward the terminal acceptor units, confirming a robust ICT process. This spatial decoupling in C8 is consistent with its narrowed band gap and favorable near-infrared (NIR) absorption profile. **C9** exhibits intermediate behavior, maintaining a high oscillator strength due to a balanced overlap between the hole and electron isosurfaces.

Since the intrinsic CT contribution is sensitive to the definition of fragments, it was not interpreted in isolation. Instead, it was evaluated alongside Δr, which reflects the electron-hole separation distance, and the λ-index, which describes the degree of spatial overlap. This multidimensional approach ensures that formal interfragment charge redistribution is accurately distinguished from genuinely spatially separated charge-transfer excitations.

Within this framework, **C1** remains the most clearly localized system in the series. Its very small Δr values for the first three excited states and relatively large λ-index values indicate substantial electron-hole overlap, which is fully consistent with its predominantly local excitation character (70.05% LE). A similar tendency is observed for C4 and C9 in their spatial descriptors. Although both compounds display moderate intrinsic CT contributions (56.02% for **C4** and 65.42% for **C9**), their small Δr values and comparatively high λ-index values show that the excitations remain spatially localized to a large extent. Thus, in these systems, the fragment-based CT component should be understood as a formal donor-acceptor redistribution rather than a strongly separated long-range charge-transfer state.

A more mixed excited-state behavior is observed for **C3**, **C5**, **C7**, and **C10**. In **C3**, the intrinsic CT contribution reaches 72.44%, yet the corresponding Δr values remain moderate and the λ-index values are not particularly low, suggesting a short-range or partially delocalized charge-transfer process rather than a fully separated CT excitation. A similar trend is observed for **C7**, which exhibits a substantial CT contribution (61.39%) yet retains appreciable electron-hole overlap. For **C5** and **C10**, the CT and LE components are more evenly balanced, with CT contributions of 53.80% and 56.39%, respectively. In both cases, the excited states are better described as mixed CT/LE transitions with noticeable polarization, rather than as purely local or strongly charge-separated states.

Table 3: Calculated Δr index, λ index, Intrinsic Charge Transfer% and Intrinsic Local Excitation% for all molecules at B3PW91/6-31+G(d,p) level.

	Δr index			**λ index**				
	1st	**2nd**	**3rd**	**1st**	**2nd**	**3rd**	**Intrinsic Charge Transfer%**	**Intrinsic Local Excitation%**
C1	0.20	0.14	0.13	0.81	0.46	0.67	29.95	70.05
C2	3.73	14.25	23.76	0.45	0.35	0.41	56.21	43.79
C3	1.19	2.15	1.35	0.67	0.38	0.65	72.44	27.56
C4	0.23	2.78	3.45	0.81	0.54	0.62	56.02	43.99
C5	0.63	5.35	4.22	0.77	0.44	0.59	53.80	46.20
C6	30.89	30.27	1.82	0.30	0.32	0.65	81.06	18.94
C7	0.52	1.79	3.73	0.80	0.57	0.63	61.39	38.61
C8	15.09	17.70	22.25	0.41	0.37	0.31	78.54	21.46
C9	0.20	0.93	0.61	0.75	0.65	0.76	65.42	34.59
C10	0.39	1.51	1.28	0.82	0.64	0.65	56.39	43.61

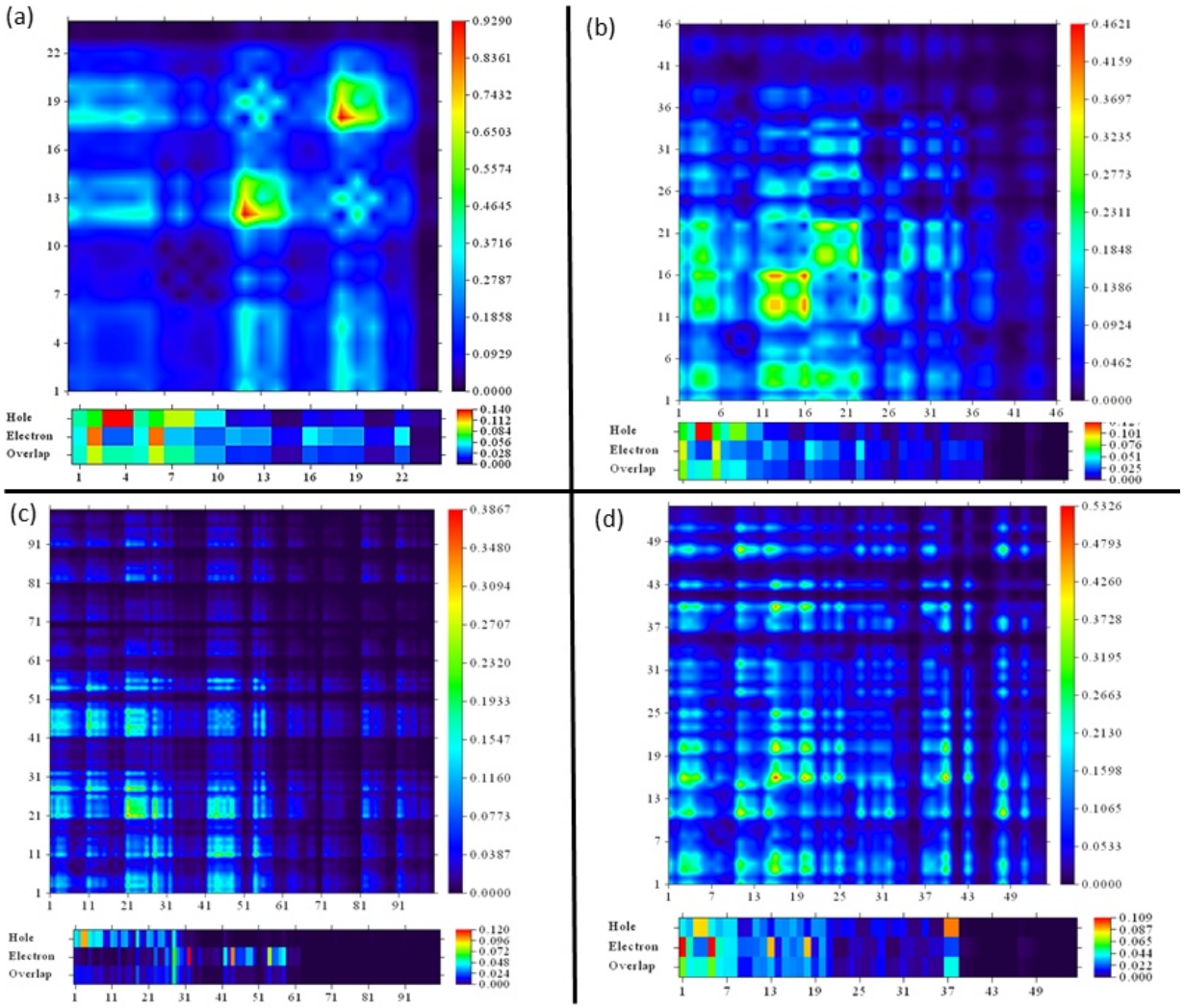

Figure 4: S1 TDM maps and S1 Hirshfeld-partitioned hole/electron distributions for S1 for of (a) **C1**, (b) **C7**, (c) **C8** and (d) **C9** at B3PW91/6-31+G(d,p) theory level.

The clearest charge-transfer character is observed for **C2**, **C6**, and **C8**. Compound **C2** already shows a marked increase in Δr from the first to the higher excited states, together with consistently low λ-index values, indicating significant charge displacement and reduced electron-hole overlap. This is in good agreement with its 56.21% CT contribution and confirms that the excitation has a clear CT-leaning character. The most pronounced CT behavior, however, is observed for **C6** and **C8**. Both

compounds exhibit exceptionally large Δr values and low λ-index values, indicating substantial spatial separation between the hole and electron densities. Their intrinsic CT contributions are also the highest in the series (81.06% for **C6** and 78.54% for **C8**), supporting the conclusion that their low-lying excited states are predominantly charge-transfer in nature.

A single pattern cannot describe the excited-state behavior of these compounds. Depending on the terminal groups and the extent of conjugative communication along the backbone, the lowest excitations may remain largely localized, adopt a mixed CT/LE character, or evolve into strongly charge-transfer-dominated states. Importantly, the combined use of Δr, λ-index, and intrinsic CT/LE percentages provides a more reliable description than any one of these descriptors alone.

3.5. Reorganization Energy and Charge-Transport Tendency

To further evaluate the charge-transport characteristics of the selected DPP-based compounds, the electron and hole reorganization energies (λ_e and λ_h) were calculated from the optimized neutral, anionic, and cationic states (Table 4). In general, lower reorganization energies are associated with smaller structural relaxation upon charge transfer and, therefore, more favorable charge-transport behavior. From this perspective, the present series shows a clear spread in transport-related performance, with some compounds exhibiting only moderate relaxation effects, while others appear markedly more suitable for either electron or hole transport.

A first broad observation is that, for most compounds, the hole reorganization energy is slightly higher than the corresponding electron reorganization energy, indicating that structural relaxation upon hole transfer is generally more pronounced than that associated with electron transfer. This trend is observed for all compounds except **C8**. Among these, **C1** shows relatively large values for both carriers, particularly for hole transport (λ_e=0.2898 eV, λ_h=0.3605 eV), suggesting comparatively unfavorable charge mobility. A similar picture is found for **C4, C5,** and **C7**, which also display relatively high reorganization energies, especially on the hole side. These results imply that, despite their acceptable optical or electronic properties in some cases, their transport performance may be limited by stronger geometric relaxation after charge injection.

Table 4: Calculated electron reorganization energies (λ_e) and hole reorganization energies (λ_h) for all molecules at B3PW91/6-31+G(d,p) level.

	λ_e	λ_h
C1	0.29	0.36
C2	0.24	0.28
C3	0.22	0.26
C4	0.23	0.31
C5	0.24	0.33
C6	0.21	0.18
C7	0.27	0.31
C8	0.03	0.02
C9	0.21	0.26
C10	0.18	0.28

A more favorable situation is found for **C3, C6, C9,** and C**10**. Compound **C3** combines relatively low and well-balanced values (λ_e=0.2197 eV and λ_h=0.2556 eV), indicating a comparatively moderate structural response for both carrier types. **C9** shows a similar behavior, with a low electron reorganization energy (0.2069 eV) and a still moderate hole value (0.2603 eV), suggesting reasonably balanced transport characteristics. In **C10**, the electron reorganization energy decreases further to 0.1811 eV, whereas the hole reorganization energy remains higher (0.2789 eV), pointing to a more favorable electron-transport tendency than hole transport. By contrast, **C6** is particularly interesting because it is one of the few compounds for which the hole reorganization energy is lower than the electron reorganization energy (λ_h=0.1833 eV vs λ_e=0.2121 eV). This suggests that **C6** may be better suited for hole transport, which is fully consistent with its donor-oriented character discussed above.

The most remarkable case in the present set is clearly **C8**, which exhibits exceptionally small reorganization energies for both carriers (λ_e=0.0327 eV and λ_h=0.0203 eV). These values are much lower than those of the remaining compounds, indicating that charge injection causes only minimal structural distortion in this molecule. Such a result points to an unusually rigid and transport-favorable electronic framework, and suggests that **C8** may support both electron and hole transfer with very limited energetic penalty. Even without extending the discussion to explicit mobility calculations, the very small reorganization energies of **C8** distinguish it from the rest of the series and reinforce its overall favorable optoelectronic profile.

Overall, the reorganization energy analysis suggests that **C1, C4, C5,** and **C7** are less favorable from a charge-transport perspective due to their relatively larger structural relaxation, whereas C3, C6, C9, and C10 exhibit more moderate, and therefore more promising, transport-related behavior. Among these compounds, **C6** appears especially favorable for hole transport, while **C10** is more favorable for electron transport. Compound **C8** stands apart from the entire series by displaying notably low reorganization energies for both carrier types, making it the most favorable candidate within the present molecular set at the intrinsic molecular level.

3.6. Effect of Molecular Skeleton on The Optoelectronic Behavior

Although all compounds investigated in this study share the same DPP-centered core, their overall electronic behavior varies markedly with the nature of the terminal skeletons and the type of π-conjugated bridge connecting these units to the central framework. In this respect, the present series clearly shows that the properties of DPP-based semiconductors cannot be explained solely by the common DPP core; rather, the terminal fragments and bridge identity largely determine whether the final structure behaves as a more localized, donor-

like, acceptor-biased, or strongly charge-transfer-active system.

The simplest case is represented by **C1**, in which the DPP core is connected to relatively weakly interacting terminal phenyl groups without a strongly polarizing end-group motif. As a result, the electronic structure remains more localized, the LUMO is less effectively stabilized, and the HOMO-LUMO gap remains the widest in the series. Thus, **C1** may be regarded as the least polarized and most localized scaffold among the investigated compounds. A different situation is found for **C2**, **C4**, and **C7**, which occupy a more intermediate position. In these structures, the peripheral units introduce a noticeable degree of donor-acceptor imbalance, but not to the extent required to produce the most strongly acceptor-dominated or most spatially separated charge-transfer states. Their behavior is therefore better described as electronically mixed, with the terminal skeletons inducing moderate polarization rather than a fully dominant donor or acceptor role.
More pronounced acceptor-side effects are observed for **C3**, **C5**, and especially **C8**. In these compounds, the terminal fragments are not merely substituents in the narrow sense, but electronically active end-group skeletons that significantly contribute to frontier-orbital modulation. This leads to stronger LUMO stabilization, narrower gaps, and more favorable low-energy absorption. In **C3**, the terminal framework already produces a clear acceptor-biased profile, although the corresponding excitation remains more short-range or partially delocalized than fully long-range in character. Compound **C5** shows a similar but slightly less extreme tendency, combining appreciable acceptor-side stabilization with mixed CT/LE behavior. The strongest case is **C8**, in which the terminal acceptor framework dominates the low-energy electronic structure and gives rise to the lowest LUMO level, the smallest band gap, the most red-shifted absorption, and one of the clearest charge-transfer signatures in the series. In this sense, **C8** represents the most strongly acceptor-biased scaffold among the investigated molecules.

A distinct pattern is observed for **C6**, **C9**, and **C10**, which remain the most relevant compounds for donor-side photovoltaic discussion. These structures show that donor-like behavior in the DPP family is not controlled solely by HOMO depth but by the balance among terminal polarization, optical response, and energetic compatibility with the acceptor. Within this subset, **C9** appears as the most balanced donor-like scaffold, combining favorable frontier orbital alignment with a relatively moderate degree of polarization. **C10** remains donor-relevant in photovoltaic terms, but its terminal framework introduces a more polarized excited-state character than that of **C9**. **C6**, by contrast, is distinguished primarily by its very strong optical response and pronounced charge-transfer behavior, showing that donor-like classification in a photovoltaic context does not necessarily imply a weakly polarized or purely local electronic structure.

Beyond the fundamental electronic properties, the distinct characteristics of **C8** and **C10** suggest specialized roles in next-generation devices. Specifically, **C8**—with its narrowest energy gap, deeply stabilized LUMO level, and pronounced red-shifted absorption—emerges as a compelling candidate for near-infrared (NIR) photodetectors and ambipolar transistors. Its high charge-transfer character and low reorganization energy suggest favorable conditions for charge separation and transport at the molecular level. On the other hand, the favorable frontier-orbital profile of **C10**, together with its relatively low electron reorganization energy, supports its potential as an electron-transporting organic semiconductor. These findings show that strategic terminal-group engineering can tune DPP derivatives from localized excitation-dominated systems to electronically distinct materials with enhanced charge-transfer and transport-related characteristics.

Overall, the present series demonstrates that the electronic diversity of DPP-based semiconductors is largely governed by terminal-skeleton engineering. Relatively small structural variations in the end-group framework and bridge identity are sufficient to shift a DPP-based system from a localized wide-gap structure to an intermediate mixed form, an acceptor-biased semiconductor, or a donor-like but still strongly polarized photovoltaic candidate. This structural sensitivity explains why compounds within the same broader DPP family can nevertheless exhibit markedly different optoelectronic, excited-state, and transport properties.

Taken together, the present series does not support a single uniform donor–acceptor interpretation. Instead, terminal-skeleton engineering generates electronically distinct subsets: **C8** stands out as the most acceptor-biased and NIR-relevant candidate, **C10** as a favorable electron-transporting system, and **C9** as the most balanced donor-like molecule within the fullerene-referenced photovoltaic framework.

4. CONCLUSION

In this study, a comparative DFT/TD-DFT framework was applied to clarify the structure–property relationships of ten DPP-based semiconductors. The benchmark results identified B3PW91/6-31+G(d,p) as the most suitable computational level for the present molecular set, providing the best overall agreement with the experimental frontier orbital energies of **C10**. The results further showed that terminal-skeleton engineering strongly governs frontier orbital alignment, optical absorption, excited-state character, and charge-transport tendencies across the series. While most compounds retained largely planar backbones, localized torsional variations acted as important modulators of π-conjugation. Among the investigated systems, **C8** emerged as the most acceptor-biased and NIR-relevant candidate because of its narrow gap, pronounced charge-transfer character, and remarkably low reorganization energies. **C10** stood out as a favorable electron-transporting system owing to its relatively low electron reorganization energy, whereas **C9** appeared as the most balanced donor-like molecule within the fullerene-referenced photovoltaic framework. Overall, the present results show that DPP derivatives should not be interpreted within a single uniform donor–acceptor picture; instead, relatively small terminal-structure changes generate electronically distinct subsets with different optoelectronic roles. These findings provide a

consistent basis for the evaluation and future design of application-specific DPP-based organic semiconductors.

5. CONFLICT OF INTEREST

The authors declare no conflict of interest.

6. ACKNOWLEDGMENTS

The authors gratefully acknowledge the computational resources provided by TÜBİTAK ULAKBİM High Performance and Grid Computing Center (TRUBA).

7. REFERENCES

1. Sayigh A. Transition towards a carbon free future [Internet]. Sayigh A, editor. Cham: Springer Nature Switzerland; 2024. (Innovative Renewable Energy). Available from: <URL>.

2. Bulavko G. Organic photovoltaics: A journey through time, advancements, and future opportunities. Hist Sci Technol [Internet]. 2024 Jun 30;14(1):10–32. Available from: <URL>.

3. Yuan J, Zhang Y, Zhou L, Zhang G, Yip HL, Lau TK, et al. Single-junction organic solar cell with over 15% efficiency using fused-ring acceptor with electron-deficient core. Joule [Internet]. 2019 Apr 17;3(4):1140–51. Available from: <URL>.

4. Caldera-Cruz E, Raveendran R, Karpov Y, Talnack F, Voit B, Kiriy A, et al. Morphology, crystallinity, and electrical performance of solution-processed OFETs based on a DPP-based small molecule. ACS Appl Electron Mater [Internet]. 2025 Aug 12;7(15):6874–84. Available from: <URL>.

5. Yu M, Wan ZC, Song SW, Yang ZY, Suzuki M, Yamada H. Dual-benefit strategy for developing an efficient photodetector with prompt response to UV-near IR radiations: *In situ* synthesis and crystallization through a simple one-step annealing. J Mater Chem A [Internet]. 2024 Jul 30;12(30):19288–97. Available from: <URL>.

6. Zhu L, Zhang M, Zhou Z, Zhong W, Hao T, Xu S, et al. Progress of organic photovoltaics towards 20% efficiency. Nat Rev Electr Eng [Internet]. 2024 Aug 21;1(9):581–96. Available from: <URL>.

7. Yue Q, Liu W, Zhu X. n-type molecular photovoltaic materials: Design strategies and device applications. J Am Chem Soc [Internet]. 2020 Jul 8;142(27):11613–28. Available from: <URL>.

8. Luo N, Zhang G, Liu Z. Keep glowing and going: Recent progress in diketopyrrolopyrrole synthesis towards organic optoelectronic materials. Org Chem Front [Internet]. 2021 Aug 10;8(16):4560–81. Available from: <URL>.

9. Liu Q, Bottle SE, Sonar P. Developments of diketopyrrolopyrrole-dye-based organic semiconductors for a wide range of applications in electronics. Adv Mater [Internet]. 2020 Jan 3;32(4):1903882. Available from: <URL>.

10. Grzybowski M, Gryko DT. Diketopyrrolopyrroles: Synthesis, reactivity, and optical properties. Adv Opt Mater [Internet]. 2015 Mar 23;3(3):280–320. Available from: <URL>.

11. Wang B, Hu X, Sun F, Yang Z, Huang W. Advanced strategic constructions of diketopyrrolopyrrole derivatives-based organic semiconducting phototheranostics. Interdiscip Med [Internet]. 2023 Jan 23;1(1):e20220010. Available from: <URL>.

12. Bao WW, Li R, Dai ZC, Tang J, Shi X, Geng JT, et al. Diketopyrrolopyrrole (DPP)-based materials and its applications: A review. Front Chem [Internet]. 2020 Sep 10;8:679. Available from: <URL>.

13. Zhao C, Guo Y, Zhang Y, Yan N, You S, Li W. Diketopyrrolopyrrole-based conjugated materials for non-fullerene organic solar cells. J Mater Chem A [Internet]. 2019 Apr 24;7(17):10174–99. Available from: <URL>.

14. Meng D, Zheng R, Zhao Y, Zhang E, Dou L, Yang Y. Near-infrared materials: The turning point of organic photovoltaics. Adv Mater [Internet]. 2022 Mar 20;34(10):2107330. Available from: <URL>.

15. Molina D, Álvaro-Martins MJ, Sastre-Santos Á. Diketopyrrolopyrrole-based single molecules in photovoltaic technologies. J Mater Chem C [Internet]. 2021 Nov 25;9(45):16078–109. Available from: <URL>.

16. Tang A, Zhan C, Yao J, Zhou E. Design of diketopyrrolopyrrole (DPP)-based small molecules for organic-solar-cell applications. Adv Mater [Internet]. 2017 Jan 9;29(2):1600013. Available from: <URL>.

17. Bredas JL. Mind the gap! Mater Horizons [Internet]. 2014 Nov 19;1(1):17–9. Available from: <URL>.

18. Taouali W, Casida ME, Darghouth AAMHM, Alimi K. Theoretical design of new small molecules with a low band-gap for organic solar cell applications: DFT and TD-DFT study. Comput Mater Sci [Internet]. 2018 Jul 1;150:54–61. Available from: <URL>.

19. Mestiri T, Alimi K. DFT and TD-DFT design of small π-conjugated molecules with narrow band gap and high efficiency for organic solar cells. Theor Chem Acc [Internet]. 2018 Oct 8;137(10):133. Available from: <URL>.

20. Celik S, Ergun Y, Alp S. Synthesis and spectroscopic studies of 3,6-Diphenyl-2,5-Dihydropyrrolo[3,4-C]Pyrrole-1,4-Dion's N,N'-Dialkyl derivatives. J Fluoresc [Internet]. 2009 Sep 24;19(5):829–35. Available from: <URL>.

21. Yemene AE, Venkatraman V, Moe Almenningen D, Hoff BH, Gautun OR. Synthesis of novel 3,6-Dithienyl diketopyrrolopyrrole dyes by direct C-H arylation. Molecules [Internet]. 2020 May 18;25(10):2349. Available from: <URL>.

22. Josse P, Dalinot C, Jiang Y, Dabos-Seignon S, Roncali J, Blanchard P, et al. Phthalimide end-capped thienoisoindigo and diketopyrrolopyrrole as non-fullerene molecular acceptors for organic solar cells. J Mater Chem A [Internet]. 2016 Dec 15;4(1):250–6. Available from: <URL>.

23. Zhou R, Li QD, Li XC, Lu SM, Wang LP, Zhang CH, et al. A solution-processable diketopyrrolopyrrole dye molecule with (fluoronaphthyl)thienyl endgroups for organic solar cells. Dye Pigment [Internet]. 2014 Feb 1;101:51–7. Available from: <URL>.

24. Manninen VM, Heiskanen JP, Pankov D, Kastinen T, Hukka TI, Hormi OEO, et al. The effect of diketopyrrolopyrrole (DPP) group inclusion in p-cyanophenyl end-capped oligothiophene used as a dopant in P3HT:PCBM BHJ solar cells. Photochem Photobiol Sci [Internet]. 2014 Oct 1;13(10):1456–68. Available from: <URL>.

25. Yadagiri B, Narayanaswamy K, Srinivasa Rao R, Bagui A, Datt R, Gupta V, et al. D−π–A−π–D structured diketopyrrolopyrrole-based electron donors for solution-processed organic solar cells. ACS Omega [Internet]. 2018 Oct 31;3(10):13365–73. Available from: <URL>.

26. Almodôvar VAS, Tomé AC. A convenient synthesis of diketopyrrolopyrrole dyes. Molecules [Internet]. 2021 Aug 6;26(16):4758. Available from: <URL>.

27. Fusco S, Barra M, Gontrani L, Bonomo M, Chianese F, Galliano S, et al. Novel thienyl DPP derivatives functionalized with terminal electron-acceptor groups: Synthesis, optical properties and OFET performance. Chem – A Eur J [Internet]. 2022 May 2;28(25):e202104552. Available from: <URL>.

28. Heinrichová P, Pospíšil J, Stříteský S, Vala M, Weiter M, Toman P, et al. Diketopyrrolopyrrole-based organic solar cells functionality: The role of orbital energy and crystallinity. J Phys Chem C [Internet]. 2019 May 9;123(18):11447–63. Available from: <URL>.

29. Ryan JW, Matsuo Y. Increased efficiency in small molecule organic solar cells through the use of a 56-π electron acceptor – methano indene fullerene. Sci Rep [Internet]. 2015 Feb 9;5(1):8319. Available from: <URL>.

30. Frisch MJ, Trucks GW, Schlegel HB, Scuseria GE, Robb MA, Cheeseman JR, et al. Gaussian 16, Revision B.01 [Internet]. Wallingford CT: Gaussian, Inc.; 2019. Available from: <URL>.

31. Dennington R, Keith TA, Millam JM. GaussView 6.0. 16. Semichem Inc., Shawnee Mission [Internet]. 2016. Available from: <URL>.

32. Scharber MC, Mühlbacher D, Koppe M, Denk P, Waldauf C, Heeger AJ, et al. Design rules for donors in bulk-heterojunction solar cells—towards 10 % energy-conversion efficiency. Adv Mater [Internet]. 2006 Mar 17;18(6):789–94. Available from: <URL>.

33. Green MA. Solar cell fill factors: General graph and empirical expressions. Solid State Electron [Internet]. 1981 Aug 1;24(8):788–9. Available from: <URL>.

34. Biswas AK, Das A, Ganguly B. The influence of noncovalent interactions in metal-free organic dye molecules to augment the efficiency of dye sensitized solar cells: A computational study. Int J Quantum Chem [Internet]. 2017 Sep 15;117(18):e25415. Available from: <URL>.

35. Deng WQ, Sun L, Huang JD, Chai S, Wen SH, Han KL. Quantitative prediction of charge mobilities of π-stacked systems by first-principles simulation. Nat Protoc [Internet]. 2015 Apr 26;10(4):632–42. Available from: <URL>.

36. Qiu M, Pei W, Lu Q, Li Z, Li Y, Liang J. DFT characteristics of charge transport in DBTP-based hole transport materials. Appl Sci [Internet]. 2019 May 31;9(11):2244. Available from: <URL>.

37. Bourass M, Benjelloun AT, Benzakour M, Mcharfi M, Hamidi M, Bouzzine SM, et al. The computational study of the electronic and optoelectronics properties of new materials based on thienopyrazine for application in dye solar cells. J Mater Environ Sci [Internet]. 2016;7(3):700–12. Available from: <URL>.

38. Lu T. A comprehensive electron wavefunction analysis toolbox for chemists, Multiwfn. J Chem Phys [Internet]. 2024 Aug 28;161(8):082503. Available from: <URL>.

39. Stewart JJP. Optimization of parameters for semiempirical methods V: Modification of NDDO approximations and application to 70 elements. J Mol Model [Internet]. 2007 Dec 9;13(12):1173–213. Available from: <URL>.

40. Chai JD, Head-Gordon M. Long-range corrected hybrid density functionals with damped atom–atom dispersion corrections. Phys Chem Chem Phys [Internet]. 2008 Nov 28;10(44):6615–20. Available from: <URL>.

41. Hehre WJ, Ditchfield R, Pople JA. Self—consistent molecular orbital methods. XII. Further extensions of gaussian—type basis sets for use in molecular orbital studies of organic molecules. J Chem Phys [Internet]. 1972 Mar 1;56(5):2257–61. Available from: <URL>.

42. Lee C, Yang W, Parr RG. Development of the colle-salvetti correlation-energy formula into a functional of the electron density. Phys Rev B [Internet]. 1988 Jan 15;37(2):785–9. Available from: <URL>.

43. Yanai T, Tew DP, Handy NC. A new hybrid exchange–correlation functional using the coulomb-attenuating method (CAM-B3LYP). Chem Phys Lett [Internet]. 2004 Jul 21;393(1–3):51–7. Available from: <URL>.

44. Hariharan PC, Pople JA. The influence of polarization functions on molecular orbital hydrogenation energies. Theor Chim Acta [Internet]. 1973 Sep;28(3):213–22. Available from: <URL>.

45. Krukau A V., Vydrov OA, Izmaylov AF, Scuseria GE. Influence of the exchange screening parameter on the performance of screened hybrid functionals. J Chem Phys [Internet]. 2006 Dec 14;125(22):224106. Available from: <URL>.

46. Perdew JP, Burke K, Ernzerhof M. Generalized gradient approximation made simple. Phys Rev Lett [Internet]. 1996 Oct 28;77(18):3865. Available from: <URL>.

47. Perdew JP, Burke K, Ernzerhof M. Generalized Gradient Approximation Made Simple. Phys Rev Lett

[Internet]. 1997 Oct 28;78:1396. Available from: <URL>.

48. Adamo C, Barone V. Exchange functionals with improved long-range behavior and adiabatic connection methods without adjustable parameters: The mPW and mPW1PW models. J Chem Phys [Internet]. 1998 Jan 8;108(2):664–75. Available from: <URL>.

49. Becke AD. Density-functional thermochemistry. III. The role of exact exchange. J Chem Phys [Internet]. 1993 Apr 1;98(7):5648–52. Available from: <URL>.

50. Clark T, Chandrasekhar J, Spitznagel GW, Schleyer PVR. Efficient diffuse function-augmented basis sets for anion calculations. III. The 3-21+G basis set for first-row elements, Li–F. J Comput Chem [Internet]. 1983 Sep 7;4(3):294–301. Available from: <URL>.

51. Krishnan R, Binkley JS, Seeger R, Pople JA. Self-consistent molecular orbital methods. XX. A basis set for correlated wave functions. J Chem Phys [Internet]. 1980 Jan 1;72(1):650–4. Available from: <URL>.